

Design, Fabrication, Calibration and Testing of Shock Tube Impulse Test Facility

Abhishek Kamal, Vinayak Kulkarni, Niranjana Sahoo

Abstract

Ground-based testing facilities are very crucial and helpful in conducting experiments for various aerodynamics studies such as flow analysis, estimation of aerodynamic forces, heat transfer analysis etc. As the initial phase of the study, similar to the available ground-based facility, a shock tube has been designed with different geometrical configurations to conduct the experiments with different aerodynamic test models at several test conditions. Each section of the designed shock tube is further fabricated with SS304 stainless steel material by keeping safety in mind under high-pressure working conditions. Before conducting experiments in a shock tube, a calibration experiment is important to understand the workings of the shock tube by estimating the shock tube parameters such as Shock Mach Number, Reflected Shock Mach Number, etc. After completion of calibration, an aerodynamic drag force study is performed to test this facility. For this, initially, an experiment was conducted with piezofilms-based stress wave force balance along with the hemispherical model by mounting at the end of the shock tube. Dynamic calibration of model-balance assembly is also performed to estimate the System Response Function by employing the well-developed force prediction algorithm, i.e., De-convolution and ANFIS after training. A trained algorithms are further used to predict the drag force over the designed test model from strain-time history responses. This Chapter mainly focused on the design, fabrication, and calibration of a new shock tube facility. Testing of the shock tube facility has been done in a simple manner.

1. Introduction

In the domain of high-speed aerodynamics, shock waves are recognized as a crucial aspect of flow field characteristics. In extremely powerful occurrences, shock waves may pass through any material, including plasma, electromagnetic fields, solids, liquids, and gases. These shock waves compress the medium which changes the properties of the medium drastically. This capacity of shock waves to produce an immediate rise in medium properties such as pressure and temperature and further these changes in properties forms various free stream conditions and usage in different areas of research, i.e., aerospace applications, industrial and medical research areas. In the eighteenth century, many experiments and studies were conducted, and it was concluded that the waves generated by explosions were much quicker than sound waves speed. Initially, shock tubes were fabricated using inexpensive materials that could produce a pressure pulse through the explosion [1]. Supersonic/hypersonic wind tunnels and other readily available facilities were used to study the high-speed, and altitude flows from an aerodynamic standpoint. The development of shock wave capabilities led to the development of high enthalpy short-duration impulse facilities to mitigate the adverse effects of re-entry and scramjet engines. However, these facilities could only supply a limited quantity of data since they lacked flow

diagnostic equipment and high-speed sensors. It is now possible to create hypersonic flows with a somewhat substantial impulse facility for a brief test duration of a few milliseconds because of recent developments in high-speed data-capturing equipment. Even while short test spans provide challenges for processing data accumulating, there is a necessary resolution for the intended time span made possible by contemporary high-speed equipment and flow diagnostic procedures. These short-span facilities are appealing because they can generate a high enthalpy slug of test gas at a low cost. Over the last few decades, the facilities have included both minor and major upgrades to their explosion tubes, free piston shock tunnels, and shock tunnels [2, 3, 4, 5]. The most basic device that may produce movable shock waves when a high-pressure region abruptly encounters a low-pressure region is a shock tube. A "shock tube" is a laboratory equipment that may be used to scientifically reproduce many comparable natural phenomena related to shock-associated/shock wave physics because shock waves can be produced under controlled conditions. A diaphragm separates the two portions of the shock tube, which are often closed pieces of equipment. The driver (region "4"), and the driven (region "1"), are the two sections. The pressure circumstances at which each segment is filled cause the diaphragm to rupture; these pressure values are known as the bursting pressure for the related material. Generally, stainless steel is used to build shock tubes, and depending on the required shock wave strength, diaphragms can be formed of steel, aluminum, cellophane, or any other material. As a result, the gas from the high-pressure (driver) region of the tube expands into the test gas-containing low-pressure (driven) section. For a diaphragm part, pressure waves combine to produce the shock front upon the abrupt rupture of the diaphragm, and this front then spreads into the low-pressure region. The "contact surface," known as the interface between gases of the driven and driver section (regions "2" and "3"), respectively, in the medium, comes after the so-called "primary shock." The speed of the moving primary shock approaching a driven portion of the shock is higher than the speed of the sound wave of stagnant test gas. Because of it the test gas gets compressed, heated, and accelerated, which leads to a sharp increase in temperature and pressure (area "2"), illustrated in **Figure 1**. At this distance, the compressed medium attains the values equilibrium of temperature, density, and pressure, and the shock wave usually has a thickness of a few mean free paths. When the incident primary shock wave reaches the end of the shock tube, it gets reflected and moves back. At this stage, the test gas has established the characteristics associated with area "2" Due to the instantaneous reflection of the test gas from the shock tube end, the test gas particles have zero velocity and become stagnant for a short period of time [6]. Consequently, due to this reflection, the test gas gets compressed and heated again, which is expressed in the region '5'. After the rupturing of the diaphragm, in the driver section, a sequence of expansion waves are generated that are initiated from the diaphragm. These expansion waves further proceed towards the driven portion of the shock tube and then reflect back from the end wall of the high-pressure driver section [6] In order to prevent the driver gases from contaminating the test gases throughout test flow durations, the proper length ratio between the driver and the driven portion is maintained. The test medium in regions "2" and "5" under abruptly compressed and heated

conditions invites a number of attractive mechanical applications in the fields of chemical kinetics [7] fuel ignition delay measurements [8], impact assessment on structures [9], and studies of shock assist deformation [10]. One of the main objectives of this study is to set-up a unique shock tube facility of a reasonable scale. The establishment of this facility needs to complete some milestones, which include the estimation of the appropriate geometrical features, its fabrications, and the advanced instrumentation to gather experimental responses and calibration for its capabilities. Thus, the initial design is finished, and the complete detailed drawings are accomplished.

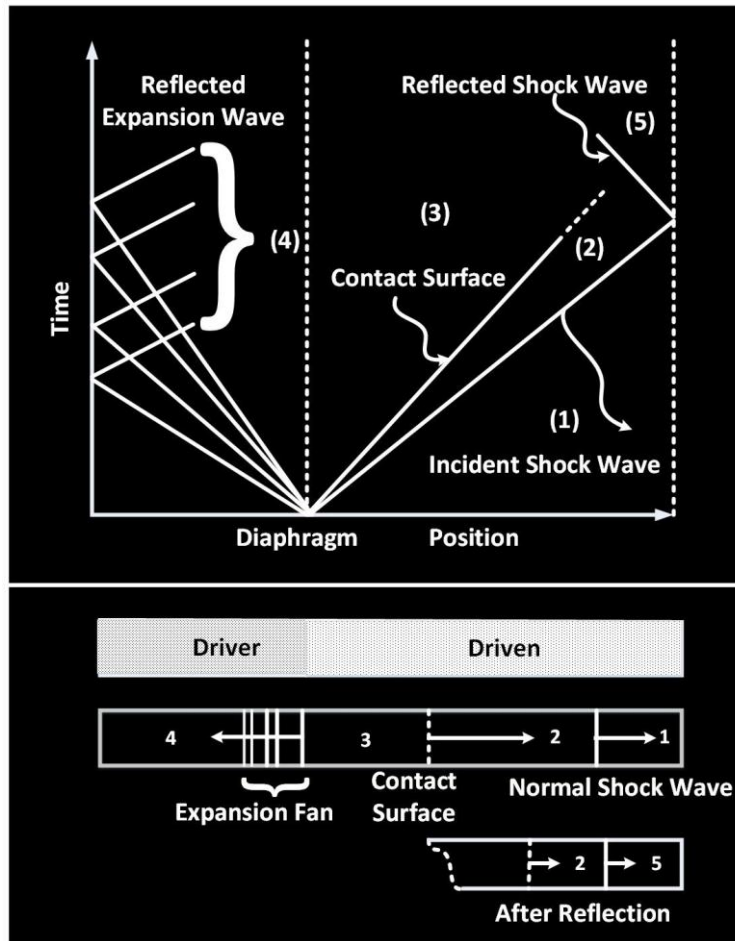


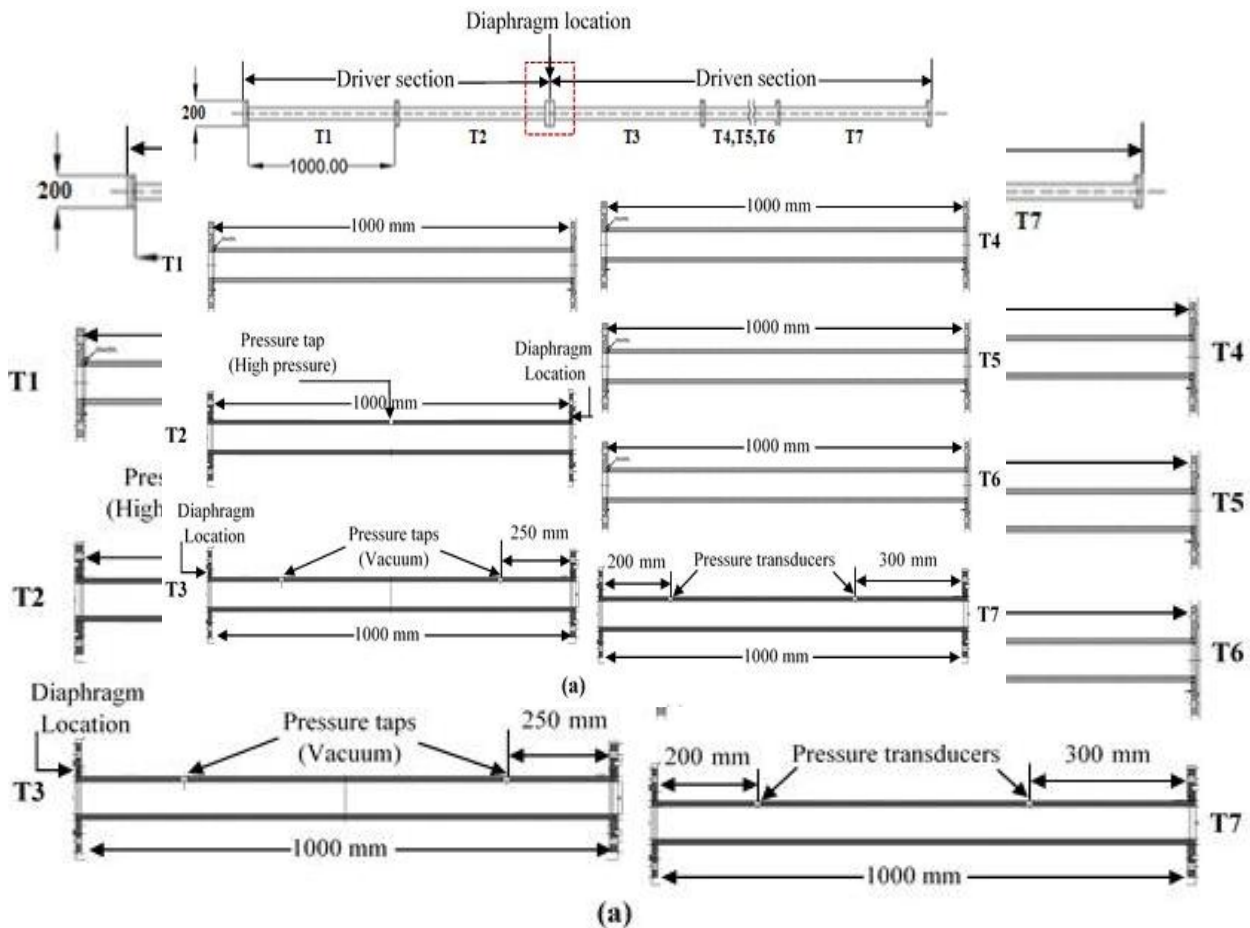
Figure 1: Schematic and working principle of conventional Shock Tube

2. Geometrical parameters for shock tube design

In general, shock tube bears a tremendous pressure rise in a short period of time. Thus, the geometrical parameters of the shock tube and the hoop stress generated during the high pressure loading conditions are decided by the theory of thick wall pressure vessel. The hoop stress (σ_x) developed at different radial distance (x) of the thick cylinder is given by

$$\sigma_x = - p_x - x \frac{dp_x}{dx} \tag{1}$$

Where, p_x is the radial compressive stress. The pressure at the inner wall of the cylinder is considered as 50 bar, which is the maximum limit for driver gas pressure after rupture of metallic diaphragm. The internal diameter of the cylinder is decided as 60 mm. By considering all the input conditions, it is observed that the hoop stress [11] of the material should not exceed 1.785 MPa. Keeping all the safety conditions in mind, it is decided to fabricate the shock tube by stainless steel (SS 304L) material [12]. The outer diameter of the shock tube is decided as 80 mm. The yield stress SS 304L material is $\sigma_{ys} = 205$ MPa [13] which is significantly higher than the estimated hoop stress. The final dimension of the shock tube facility is illustrated in **Figure 2**. Each tube of the shock tube facility is of 1000 mm length. The driver section of the shock tube is having two tubes and the driven section is with five tubes **Figure 2(a)**. Some predefined holes are allocated on the tubes for instrumentation. All the cylinders are coupled together by the male and female flanges **Figure 2 (b)**. The driver section and the driven section of the shock tube are also connected by the same coupling mechanism. However, the male and the female flanges at the diaphragm location are designed sophisticatedly for the easy mounting the metallic diaphragm **Figure 3**.



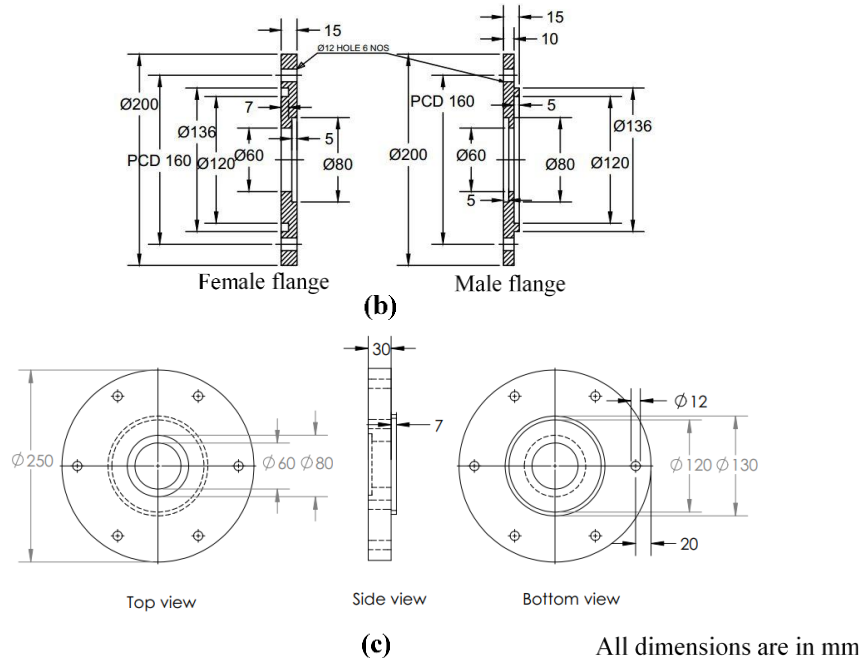


Figure 4. 2: Geometrical parameters of the (a) shock tube assembly (b) male and female flanges (c) Male and Female flange at the diaphragm locations

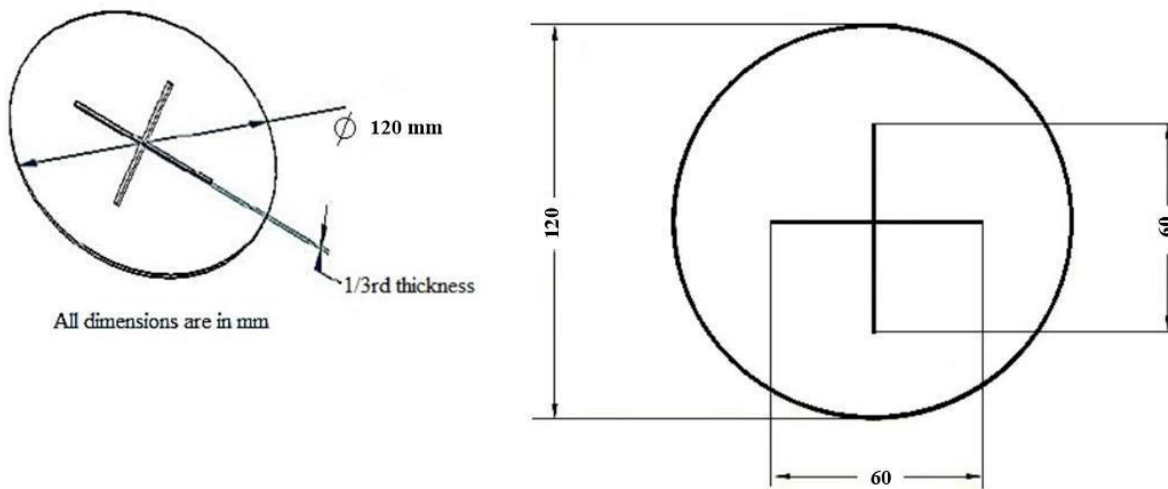
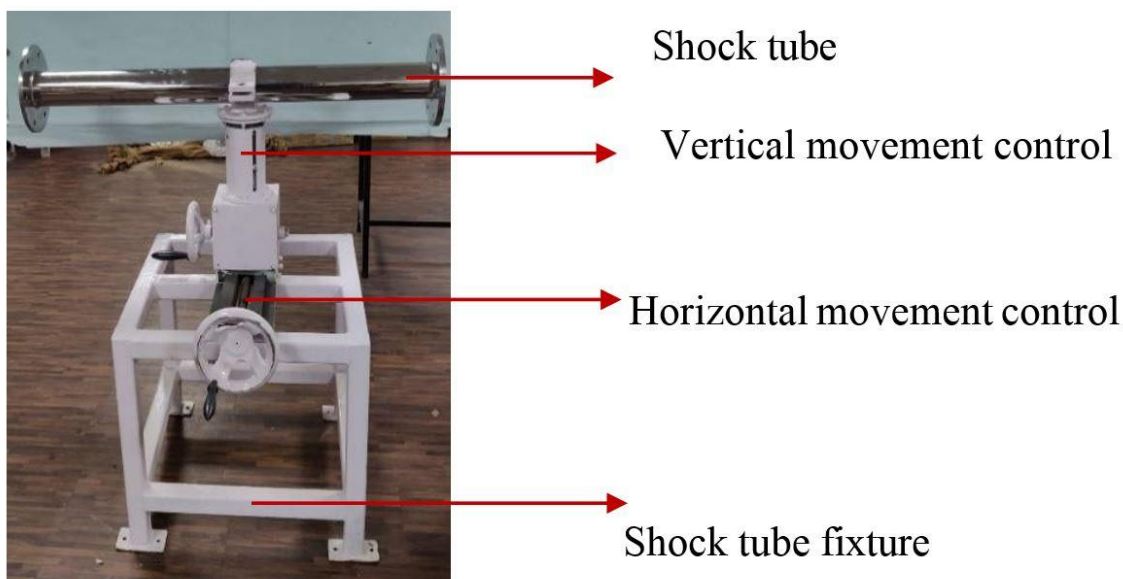


Figure 3: Schematic of the metallic diaphragm for experiment purpose

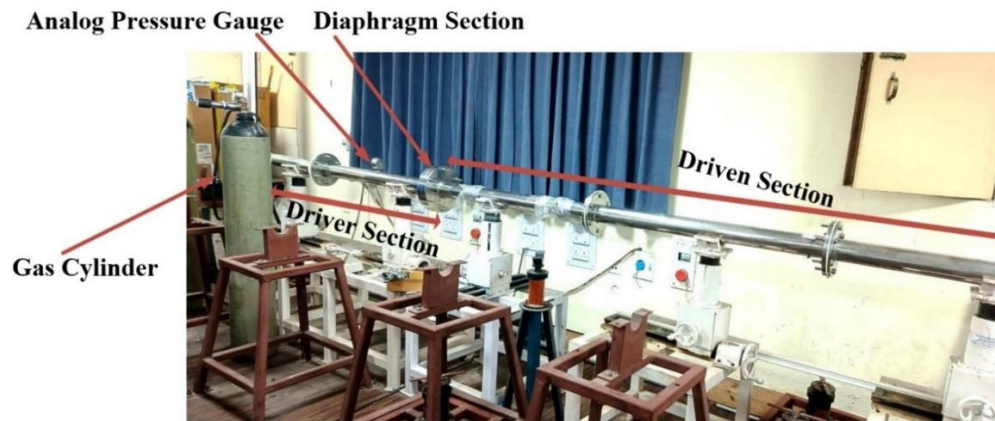
3. Installation of impulsive test facility: A Shock tube

The shock tube is made of stainless steel which is separated by two sections i.e. driver section with 1 m long and driven section respectively. It has driven section with two tubes and six tubes in the driven section. In general, the driven section has been kept longer as compared to the driver section, which ensures that the depletion of shock fronts does not show the primary concerns when it gets reflected from the end wall. Each tube has an inner diameter of 60 mm and a thickness of 10 mm. Both sections of shock tube are separated by a metallic diaphragm which is mounted at the flange. The diaphragms for the shock tube are made of aluminum

sheets, which have a diameter of 120 mm and a thickness of 1.5 mm respectively (**Figure 3**). To ensure the proper rupturing of the diaphragm, V-type grooves are generated, and the depth of the grooves is considered as one-third of the diaphragm's thickness [1]. It assures the possibility of rupturing the location of the diaphragm with less effect on stress concentration. An appropriate diaphragm thickness results as the uniformity in rupture pressure as much as possible. Furthermore, the rupture pressure does not substantially affected by the inherent impurities presence in material. The driver portion of the shock tube is filled with a gas of high pressure of gas, a pressure regulator, pressure gauges (analog and digital), and a sufficient number of valves for gas regulation. It is kept 2 m long with a ball valve, which ensure the filling of gas in a shock tube. The gas cylinder is connected to a pressure regulator which regulates the mass flow rate of the gas as well as pressure inside driver section. There are two ball valves located at the opening of cylinder, one is responsible for entering of the high-pressure gas inside the cylinder other is for exit of gas from the cylinder to the atmosphere. Driven section of the shock tube kept 5 m long. As per design, the two tubes of driven section are completely closed which other tube of driven section have lases with some important sensors such as pressure transducers, vacuum pump valve etc. The shock tube facility is fabricated in conventional lathe machine as per the designed geometrical parameters. After machining, the inner surface of the tubes are polished by honing process to acquire good surface finish, diametric roundness and axial straightness. To grip the shock tube perfectly during experiment, rigid shock tube fixtures are also designed and fabricated for each tube **Figure 4 (a)**. The fixture units are assisted with the both horizontal and vertical movement system to achieve horizontal alignment of the shock tube to the ground. The laboratorial view of installation of shock tube is shown in **Figure 4 (b)**.



(a)



(b)

Figure 4 (a) Shock tube with fixture unit **(b)** Pictorial View of Shock Tube Installation

4. Instrumentation of shock tube

Some fundamental needs for the whole calibration and experimental procedure in a shock tube include measuring the rise in pressure and speed of shock wave and further controlled the pressure ratios through the metallic diaphragm, which separates the section of the shock tube. The measurement of initial pressure inside the driven segment has been done parallel with the help of a mercury manometer, and a precision vacuum gauge. Both the driver and the driven portion of the shock tube are maintained at room temperature, which is 25°C. At the last portion of the shock tube driven side, there is two pressure sensors (PCB Piezotronics, USA; Model 113B22) have been positioned at the pressure tap sites (**Figure 2(a)**). The pressure transducers are enclosed in an SS holder (1/4 BSP thread) that is around 10.8 mm long (about the thickness of the shock tube), so these holders have been faced towards the shock tube's inner surface. When the diaphragm ruptures, the pressure sensor, which faces towards the shock tube's inner surface, measures the jumps due to pressure variation in the main and reflects shock waves. Once the primary shock travels through both sensors, a change in voltage has been addressed in the oscilloscope (Make: Tektronix (MDO34), which has a 100MHz bandwidth and a 5 GS/s sampling rate) which corresponds to a pressure jump throughout the shock wave (area "2"). When the shock waves reflect off the driven section's end flange. It travels through the previously elevated medium of higher pressure and temperature. There is a subsequent increase in pressure (In region "5"). The pressure transducer and its holder are shown in **Figure 5 (a, b)**. Moreover, a line diagram of shock tube instrumentation has been given in **Figure 5 (c)**.

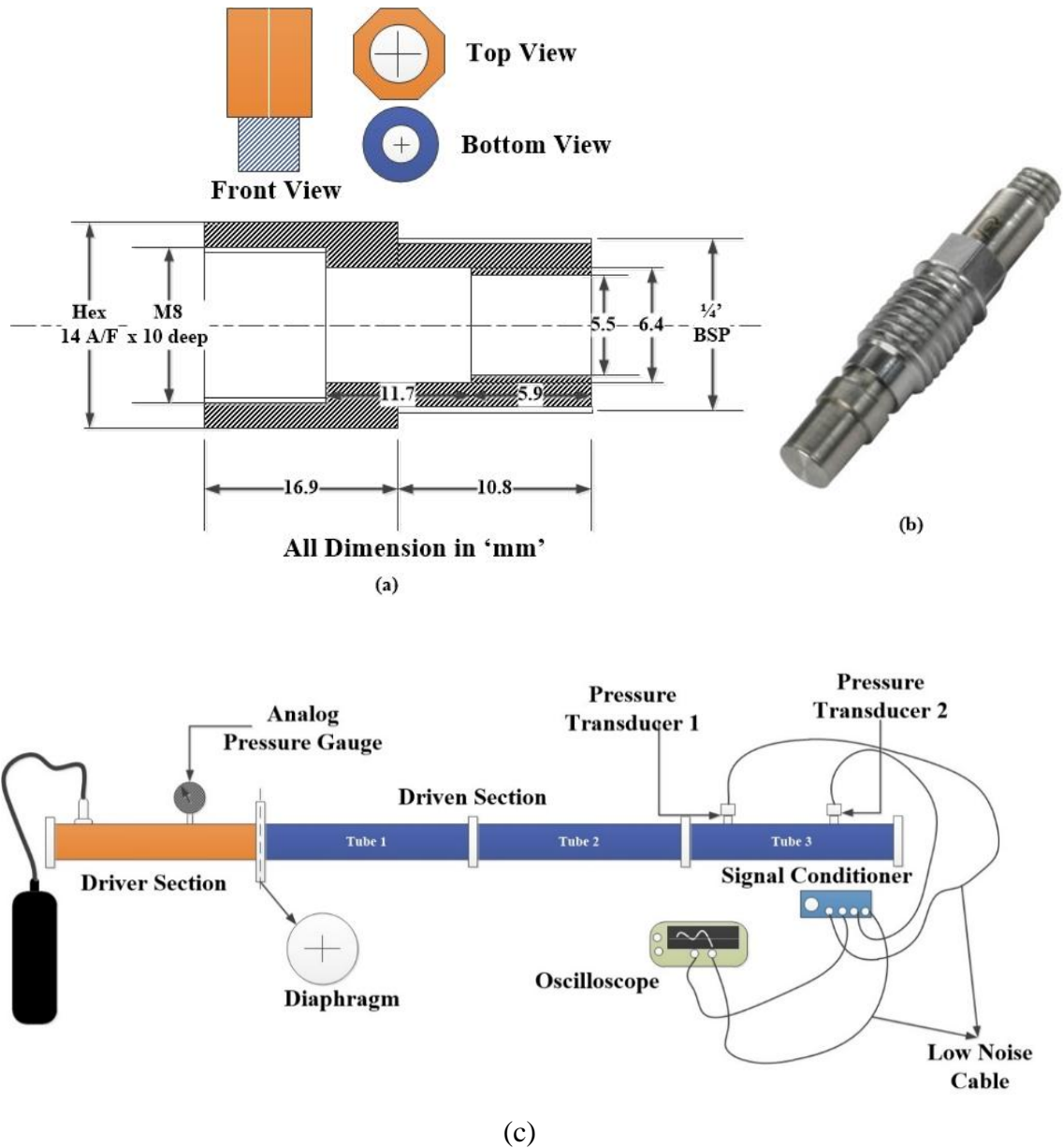


Figure 5 : (a) Schematic of Pressure transducer holder, (b) Pictorial view of Pressure transducer shock tube and (c) Line diagram of Shock tube Instrumentation

5. Calibration of Shock tube

A laboratory tool known as a constant area shock tube produces a plane shock wave as a result of rupturing the diaphragm which separates the shock tube regions i.e. high (driver) and low (driven) pressure regions respectively. An immediate burst in the diaphragm leads the high pressure gas travels into the low pressure test gas. Due to this movement, a series of compression as well as the expansion waves are generated and moves towards the driven and driver sections of the shock tube respectively. As a result, compression waves form a normal shock in driven section and it travels throughout section (**Figure 1**). Concurrently, the low-pressure driven portion also serves as the contact between the driver and driven gas (test gas). Compression shock waves are reflected back and return to the driven section of the tube as they move closer to the end of the shock tube.

Because of the cord of moving shock, the trapped test gas—which lies between the test gas and the reflected shock wave—has high pressure, temperature, and velocity in relation to the tube. The aerodynamic flow fields may be simulated by using this moving trapped area of gas at high temperature as well as elevated pressure in form of impulsive force. Nevertheless, a few milliseconds is the maximum test span for such an identical flow. The shock tube's performance must be assessed in relation to its ideal behavior before it is used in real-world applications.

6.1 Shock tube relations

From the literature, one dimensional study of shock tube has been conducted and its formal behavior can be predicted through one-dimensional Rankine-Hugonit relations [14]. As per shock tube operation regions given in **Figure. 1**. In driver section, the high pressure gas specific heat ratio is denoted by γ_4 . Similarly, the low pressure gas specific heat ratio is termed as γ_1 and both gases regions are by diaphragm mentioned also in previous sections. The pressure ratios (p_4 / p_1) and the speeds of sound (a_4 / a_1) ratios for the driver and driven sections, respectively, have a significant impact on the performance of the shock tube. The mathematical formulas for determining the elevated pressure and temperature across principal shock (p_2 / p_1) and (T_2/T_1) along with the elevated pressure and temperature across principal shock are (p_5 / p_1) and (T_5 / T_1), and reflected shock Mach number (M_R), which is a function of principal shock Mach number (M_s), are shown in **Figure 1** along with the notations used for different regions of the shock tube distinct instants. [15].

$$\frac{p_2}{p_1} = 1 + \frac{2\gamma_1}{\gamma_1 + 1} (M_s^2 - 1); \quad \frac{T_2}{T_1} = \frac{1 + \left(\frac{\gamma_1 - 1}{\gamma_1 + 1}\right) \frac{p_2}{p_1}}{1 + \left(\frac{\gamma_1 - 1}{\gamma_1 + 1}\right) \frac{p_1}{p_2}} \quad (2)$$

$$\frac{T_2}{T_1} = \frac{1 + \left(\frac{\gamma_1 - 1}{\gamma_1 + 1}\right) \frac{p_2}{p_1}}{1 + \left(\frac{\gamma_1 - 1}{\gamma_1 + 1}\right) \frac{p_1}{p_2}} \quad (3)$$

$$\frac{p_4}{p_1} = \left(\frac{p_2}{p_1}\right) \left[1 - \frac{(\gamma_4 - 1)(a_1/a_4) \left(\frac{p_2}{p_1} - 1\right)}{\left(\sqrt{2\gamma_1}\right) \left(\sqrt{(2\gamma_1) + (\gamma_1 + 1) \left(\frac{p_2}{p_1} - 1\right)}\right)} \right]^{\frac{-2\gamma_4}{(\gamma_4 - 1)}} \quad (4)$$

$$u_2 = u_3; \quad p_2 = p_3; \quad a_1 = \sqrt{\gamma_1 R_1 T_1}; \quad a_4 = \sqrt{\gamma_4 R_4 T_4} \quad (5)$$

$$\frac{p_5}{p_1} = \left[\frac{2\gamma_1 M_s^2 - (\gamma_1 - 1)}{(\gamma_1 + 1)} \right] \left[\frac{-2(\gamma_1 - 1) + M_s^2 (3\gamma_1 - 1)}{2 + M_s^2 (\gamma_1 - 1)} \right] \quad (6)$$

$$\frac{T_5}{T_1} = \left(\frac{[2(\gamma_1 - 1)M_s^2 + 3 - \gamma_1][(3\gamma_1 - 1)M_s^2 - 2(\gamma_1 - 1)]}{(\gamma_1 + 1)^2 M_s^2} \right) \quad (7)$$

$$\frac{M_R}{M_s^2 - 1} = \frac{M_s}{M_s^2 - 1} \sqrt{1 + \frac{2(\gamma_1 - 1)}{(\gamma_1 + 1)^2} (M_s^2 - 1) \left(\gamma + \frac{1}{M_s^2}\right)} \quad (8)$$

6.2 Procedure of operation of impulsive test facility

Primarily, an aluminum diaphragm with a thickness of 1.5 mm has been mounted at the diaphragm flanges. The mounting of the diaphragm ensures the clear separation of the driver and driven section. As per evidence in the literature, the strength of shock depends on the ratios of speeds of sound traveling in the medium (Driven Section), and it increases as the speed of sound increases. So, to get this, it is necessary to keep the driver gas of molecular weight while the driven gas has a low molecular weight. By doing this, the strongest shock waves can be obtained by adopting the driven gas as heavier and the driver gas as lighter. Considering these

circumstances, the current study concentrates on driver gases (nitrogen) in the shock tube-driven section with air. All of the valves are closed during the first phase of the experiment, and the driven part's (p_1) internal pressure is maintained at 1.01325 bar (atm). A high-pressure cylinder is utilized to fill the driver portion (p_4) with nitrogen, and it has been noted that the aluminum diaphragm gets ruptured around 20 bar against the low-pressure region (1.01325 bar). The design of a V-type groove plays an important role in conducting the rupturing process properly. After the sudden rupturing of the diaphragm (because of the pressure difference), a strong shock wave generates and travels throughout the driven section. According to certain aspects, the only thing that occurs when the diaphragm fails to burst correctly is the production of compression waves, which are regarded as dubious. Studies show that diaphragm cracks typically begin in the center and spread out to the margins (Takayama et al., 2014). Consequently, the gas flow begins as a jet and then, after the diaphragm's petal-like structure completely ruptures, there is a mass flow of driving gas. This controlled diaphragm rupture frequently resembles the way a series of compression waves converge to generate a shock wave. The propelled driven gas (air) experiences mass motion due to the abrupt increase in pressures across the shock wave. When it comes to the shock tube end, a reflected shock is created and travels again in the driven section. The pressure transducers, which are installed at the last segment of the driven tube, capture the pressure jumps across the primary and a reflected shock as voltage signals.

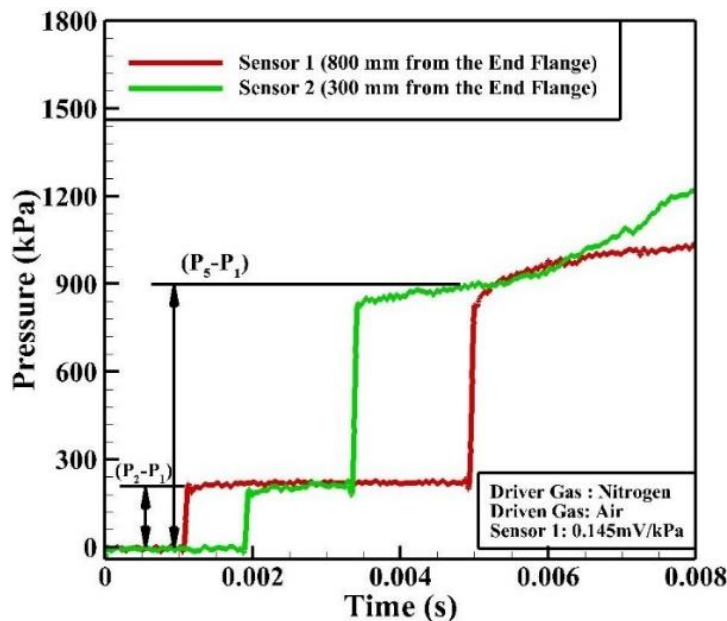


Figure 6 : Pressure variation in shock tube for an incident as well as reflected shock wave

The pressure sensors recorded the voltage signal, and it noted with "air" as the driven gas and "nitrogen" as the driver gas. The pressure rise throughout the primary and reflected shocks have been evaluated using the "sensitivity" data provided by the manufacturer, as shown in **Figure. 6**. From the known distance between the pressure taps mounted on the shock tube as well as the time travel between these pressure taps (from known

pressure responses). These known parameters help to evaluate the sound speed in the region "1" (a_1), the velocity of shock wave (V_s), and the shock Mach number (M_s, e) during the experiments from Eq. 9.

$$(9)$$

Table 1: Comparison of Principal Shock Mach number analytically as well as experimentally

Sl. No.	Driver Gas: N ₂ ; $P_1 = 1.01325 \text{ bar}; \gamma_1 = 1.4; \gamma_4 = 1.4; R_4 = 297 \text{ J (kg.K)}, R_1 = 287 \text{ J (kg.K)}$				Driven Gas: Air					
	M _s		(P ₂ /P ₁)		(P ₅ /P ₁)		(T ₂ /T ₁)		(T ₅ /T ₁)	
	Theory (M _{s,t})	Exp. (M _{s,e})	Theory (P ₂ /P ₁) _t	Exp. (P ₂ /P ₁) _e	Theory (P ₅ /P ₁) _t	Exp. (P ₅ /P ₁) _e	Theory (T ₂ /T ₁) _t	Exp. (T ₂ /T ₁) _e	Theory (T ₅ /T ₁) _t	Exp. (T ₅ /T ₁) _e
1	1.79	1.75	3.39	3.36	9.44	8.99	1.53	1.49	2.15	2.06
2	1.81	1.73	3.31	3.22	10.49	9.29	1.54	1.48	2.16	2.01
3	1.82	1.78	3.54	3.30	10.13	9.46	1.56	1.52	2.18	2.12
4	1.83	1.74	3.36	3.17	9.29	9.34	1.58	1.46	2.20	2.04

Table 2: Evaluation of shock tube parameters by using N₂ as driver gas

Sl. No.	Driver Gas: N ₂ ; $P_1 = 1.01325 \text{ bar}; \gamma_1 = 1.4; \gamma_4 = 1.4; R_4 = 297 \text{ J (kg.K)}, R_1 = 287 \text{ J (kg.K)}$			Driven Gas: Air			
	P ₄ (bar)	P ₄ / P ₁	M _s		M _R		
			Theory	Exp.	Theory	Exp.	
1	17.50	17.50	1.79	1.75	1.61	1.59	
2	18.15	18.15	1.81	1.73	1.62	1.57	
3	18.76	18.76	1.82	1.78	1.63	1.61	
4	19.38	19.38	1.83	1.74	1.64	1.58	

Table 3 : Deviation in parameters of shock tube during calibration (In Percentage)

Sl. No.	Driver Gas: N ₂				
	Percentage deviation from theoretical result				
	M _s	P ₂ /P ₁	P ₅ /P ₁	T ₂ /T ₁	T ₅ /T ₁
1	2.23	0.88	4.76	2.26	4.18
2	4.42	2.71	11.43	3.89	6.94
3	2.19	6.77	6.61	2.56	0.91
4	4.91	5.65	-0.53	8.21	7.27

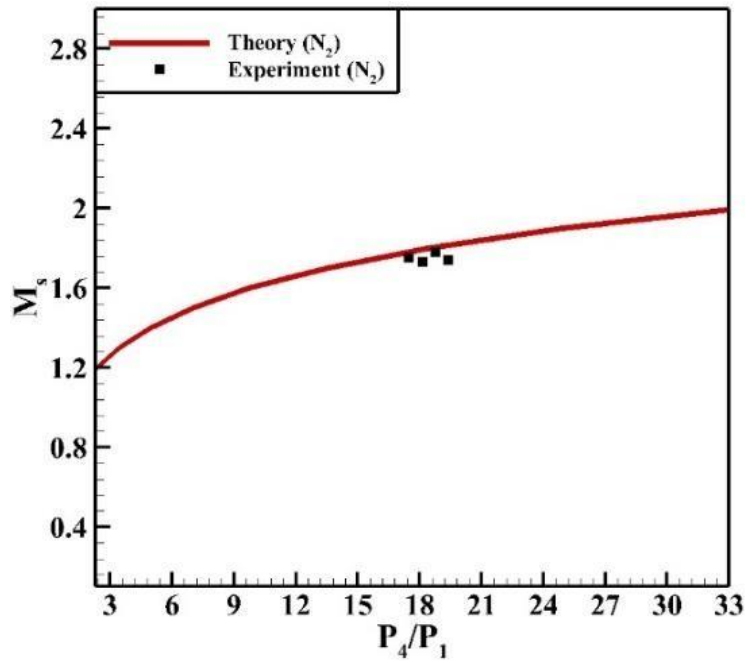


Figure 7 : Principal Shock Mach numbers comparison (experiment and theory) with pressure ratio (P_4/P_1)

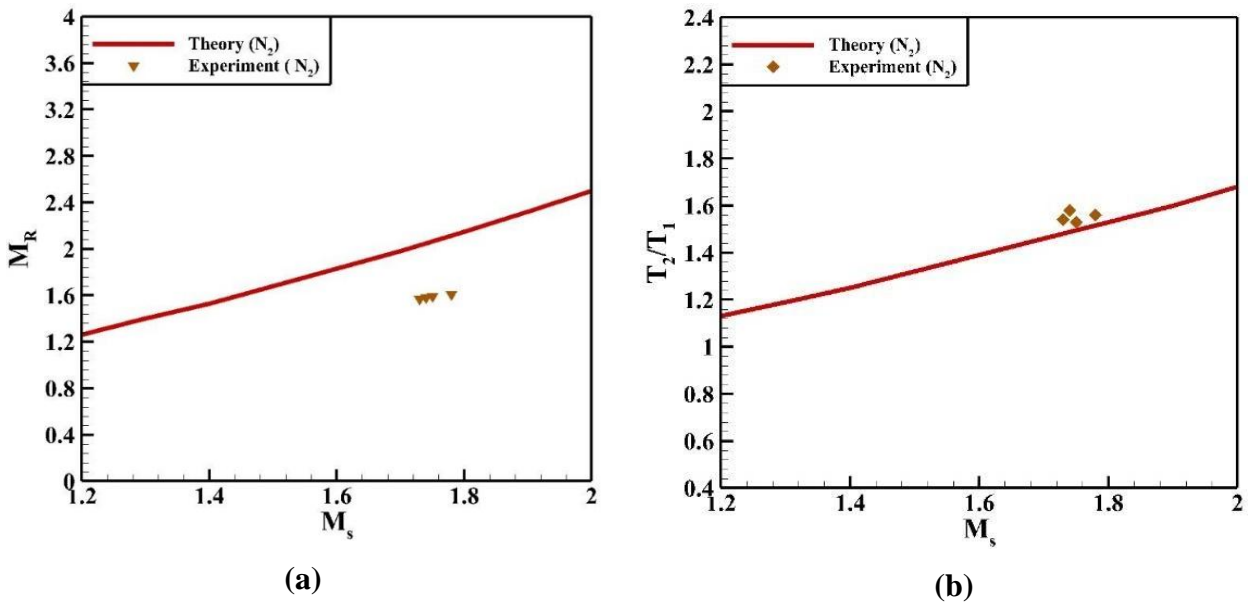


Figure 8: Variation in temperature and pressure of reflected shock wave with principal shock Mach numbers

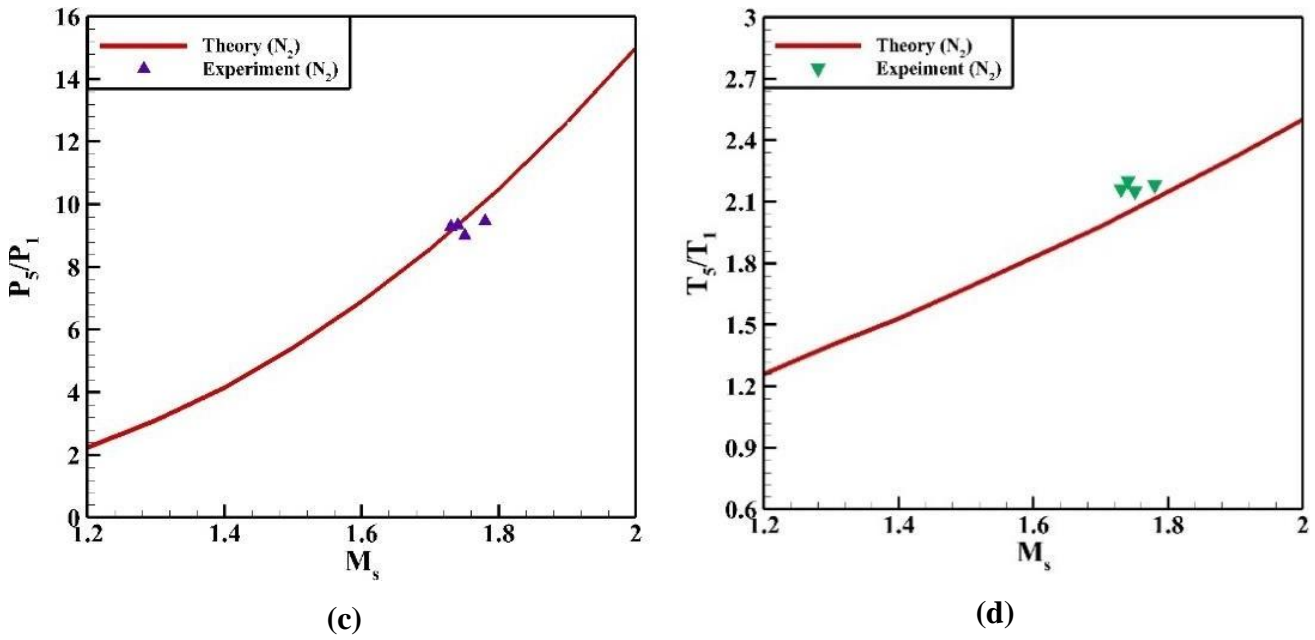


Figure 9: Variation in temperature and pressure of reflected shock wave with principal shock Mach numbers

Furthermore, Eq. 4 is used to calculate the theoretical shock Mach number ($M_{s,t}$) from initial pressure ratios (p_4/p_1) throughout the diaphragm. **Table 1** and **Figure 8** present the comparative evaluation of shock Mach numbers ($M_{s,t}$ and $M_{s,e}$) calculated from theoretical and experimental approaches with nitrogen as the driver gas (region "4" and air as the driven gas (region "1"). By using one-dimensional shock tube relations, the estimated values of $M_{s,t}$ and $M_{s,e}$, have been utilized to evaluate the theoretical as well as experimental values of pressure and temperature across principal shock [(p_2 / p_1) and (T_2 / T_1)] and reflected shock [(p_5 / p_1) and (T_5 / T_1)] by Eq. 2, 4, and Eq. 6.

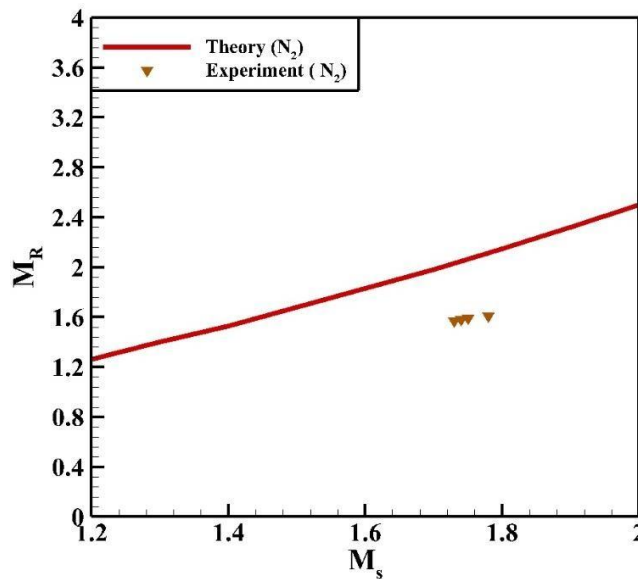


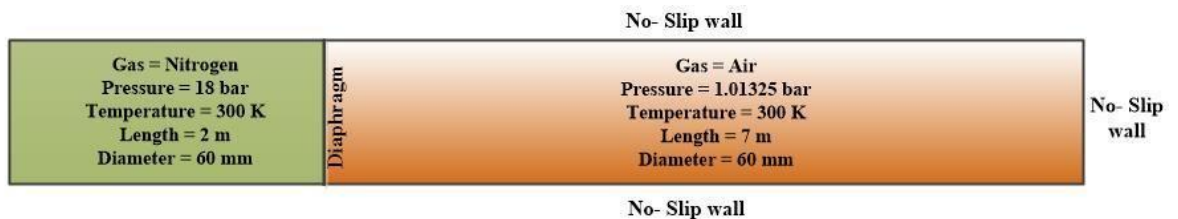
Figure 10: Variation of Mach number of reflected shock wave with Primary Mach number

These numerical values of shock tube parameters have been computed by conducting the four sets of experiments with nitrogen (N₂) as driver gas, and the comparative assessment of its behaviors are given in **Table 2 and Figure 8 (a, b) and Figure. 9 (c, d)**, respectively. At the shock end, the initial shock wave gets reflected at a very low speed because of energy loss due to impact at the end flange with a higher speed. Therefore, using Eq. 8, it is also possible to deduce the reflected shock Mach numbers (M_{R,t} and M_{R,e}) from the known values of the principal shock Mach number (M_{s,t} and M_{s,e}). Table 2 provides the values of M_{R,t}, and M_{R,e}, and Figure 10 shows the plot's trend. Furthermore, Table 3 shows the percentage deviation of each of the new shock tube facility's measured and estimated parameters. All these calibration curves (Figure 8, 9, and 10) identified as an appropriate agreement (within ±11%) between in both theoretical and experiments properties of nitrogen as driver gas. The divergence appears to be increased because different shock tube characteristics are dependent on the square of the incident shock Mach number. It should be underlined that the diaphragm's material and the development of its V-shaped groove are crucial for the creation of the correct normal and for determining the shock Mach number using the initial pressure ratio (P₄ / P₁).

6. Numerical Validation

In order to get a clear vision inside the domain, a numerical simulation has been carried out at same environmental condition. Furthermore, it also provides crucial details on the magnitude of the signals to be gathered and associated DAQ settings. So, that numerical simulation has been taken as inviscid flow throughout the domain of shock tube for better clarity. As per current investigations, ANSYS 14.5 fluent CFD solver are used to solve governing equations of flow i.e. continuity, momentum and energy through finite volume method. And, to account the effects of distinct driver and driven gases, a species transport equation has been also solved here.

Figure 11 displays the



computational domain and the corresponding preliminary flow and boundary conditions.

Figure 11: Computational domain and its boundary conditions.

To understand the real flow configuration, a complete domain has been considered and boundary of whole domain assigned as no-slip condition. A simple quadratic elements are considered for meshing of entire computational domain. The fourth order Runge-Kutta scheme with a density-based implicit solver has been selected for the transient investigation of the flow field. To evaluate the convective fluxes for the current numerical simulation, the flux vector splitting methodology known as the "advection upstream splitting method (AUSM)" has been used. And, for initialization of two distinct sections i.e. driver and driven a user defined

function (UDF) has been also incorporated for current situation. Since, rupturing of the diaphragm is not the main issue, so it assumed to burst immediately at $t = 0$. The initial flow conditions for each section and boundary conditions are shown clearly in above Figure. To find the most effective combination, simulations are run for various time steps and mesh sizes. The results obtained with the final mesh and time step selection exhibit sufficient flow field resolution and are also independent of the mesh size and time step. Lastly, the selective mesh has 427061 nodes and 420000 elements in the whole domain. The pressure distribution after the diaphragm rupture and shock reflection from the end wall are shown in **Figure 12**. From **Figure 12 (a)**, it can clearly see that the immediate rupture of the diaphragm results in a rightward movement of the incident shock wave and a leftward movement of the expansion fan, respectively.

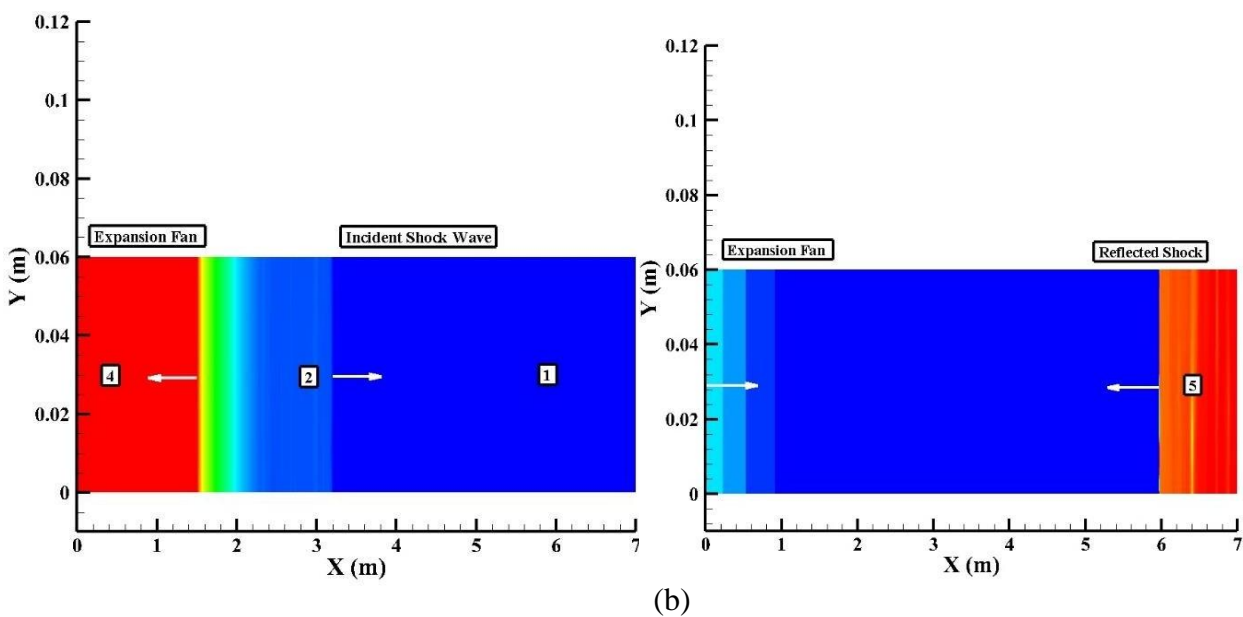


Figure 12: Pressure distribution after diaphragm rupture and shock reflection from end wall.

Further, this incident shock encountered with shock end wall and get back by creating the high pressure zone behind. The wave which reflects from the wall is termed as “Reflected Shock” that can found in **Figure 12(b)**. Since during experiment, both primary and reflected shocks are main concern, so, the essential information obtained as a result of computational efforts is the jump across these shocks, and which has been also compared with the theoretical values. Based on the CFD simulation, the pressure behind the principal shock is calculated to be 2.95 bar for the current scenarios. And, the incident shock Mach number has been found by the simulation, is 1.61. Similarly, the precise Riemann solver predicts that the principal shock Mach number and behind shock pressure are 1.52 and 2.53 bar, respectively. A strong correlation between these numbers enhances the numerical ability to show the flow conditions throughout the shock tube. So, this numerical approach can be used further to evaluate the aerodynamic force coefficients over any aerodynamic configuration under various flow environments.

7. Testing of Shock tube

8.1 Test Model and Piezofilm based Stress Wave Balance

For testing of shock tube facility, a hemispherical test model is fabricated out of aluminium with a diameter of 30 mm while a Stress Wave Force Balance (SWFB) is made of a hollow brass rod has a thickness of 1 mm and an outer diameter of 14 mm. Brass and aluminum are selected as the stress bar and test model materials, respectively, Since brass has a slower rate of stress wave propagation and aluminum has a lower density. The schematic diagram of a hemispherical model with stress wave force balance has been shown in **Figure 13**.

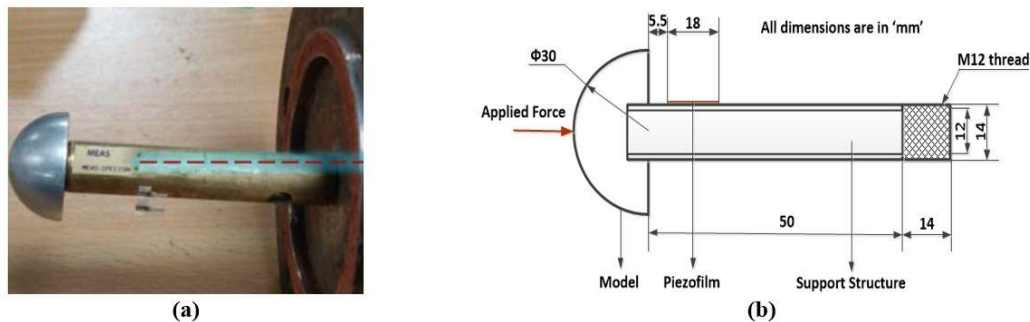


Figure 13: Schematic diagram of test Model with Stress wave Force Balance.

8.2 Force Recovery Algorithms

There are many techniques present in literature to recover the aerodynamic forces acting over aerodynamic configuration. From those techniques, here, De-convolution and ANFIS has been considered for prediction of drag force over the test model. These recovery algorithms are widely used and it's also give the closer recovery of aerodynamic force for single component force balance. Both force recovery algorithms are well described as following.

8.2.1.1 De-convolution Recovery Algorithm

As mentioned in literature, frequency domain based de-convolution algorithm is an easier and widely adopted technique for force recovery [16]. This approach employs a convolution integral between the input, output, and impulse response function by considering the dynamical system as linear. So, for evaluation of the system response function, the Fast Fourier Transforms (FFT) of the force and acceleration signals captured during calibration tests are first obtained in the frequency domain. Additionally, inverse FFT (IFFT) is used to find the recovered force time history. The strain measurement from the shock tube tests may then be used to retrieve the unknown force once the system response function is understood.

8.2.1.2 ANFIS: A soft computing based Recovery Algorithm

ANFIS (Artificial Neuro-Fuzzy Inference System), a soft computing method, has been employed currently to recover force responses for shock tube measurement tests. As discussed in the literature, Jang [17] addressed in his paper the functioning of the ANFIS algorithm, which generally integrates fuzzy logic and neural networks. In the current investigations as well, the developed aerodynamic force is derived from the recorded acceleration

signal using the same algorithm. As per the working of ANFIS, acquired force and acceleration measurements from the calibration experiments provide the input for ANFIS architecture. As it is a multi-input single-output (MISO) system, it is associated with model weights in the presence of some intermittent layers. These model weights are precisely specified by adjusting the system parameters of this ANFIS structure. These system parameters are primarily defined in the ANFIS training phase by the acquired responses during calibration experiments. A normalization of input and output data has been done with the help of the membership functions, which are selected from the literature. A hybrid-type training method is adopted to train this algorithm. Further, this trained algorithm is used for the estimation of unknown forces during the testing phase of shock tube experiments.

8.3 Result and Discussion

Initially, the calibration experiment has been performed on a hemispherical model along with Stress Wave Force Balance (SWFB) by mounting on bench vice. To perform this, a single point calibration methodology has been adopted, and the corresponding location has been shown in **Figure 4.13**. A Piezofilm sensor of PVDF type is mounted on SWFB to acquire the strain-time responses in the DAQ system. An acquired strain response corresponding to the applied calibration force is shown in **Figure 4.14**. To continue current investigations, an actual shock tube experiment has also been conducted with the same model balance assembly. The obtained strain-time responses with pressure signals are shown in **Figure 4.15**. After completion of the experiment, acquired data are processed by using available recovery algorithms. Initially, calibration experiment responses are fed into the force recovery algorithm, which is discussed in the previous section, to train it. After training, these force recovery algorithms have been validated by recovering the applied calibration force from strain responses of other calibration data. The recovered applied force from recovery algorithms is shown in **Figure 4.16**. From the figure, it has been concluded that the recovered force from the de-convolution technique gives a better prediction than ANFIS algorithms from actual calibration force. After validation, these recovery algorithms are further used to estimate the drag force over the test model from the acquired strain-time responses of shock tube experiments. The recovered drag force for shock tube experiments has been shown in **Figure 4.17**. From the figure here, it is also clearly understood that the recovered drag forces from de-convolution, as well as ANFIS, are given the approximately same magnitude, i.e., 1230 N and 1194 N, respectively. The recovered forces also follow the same trends from the same input strain responses of the shock tube experiment.

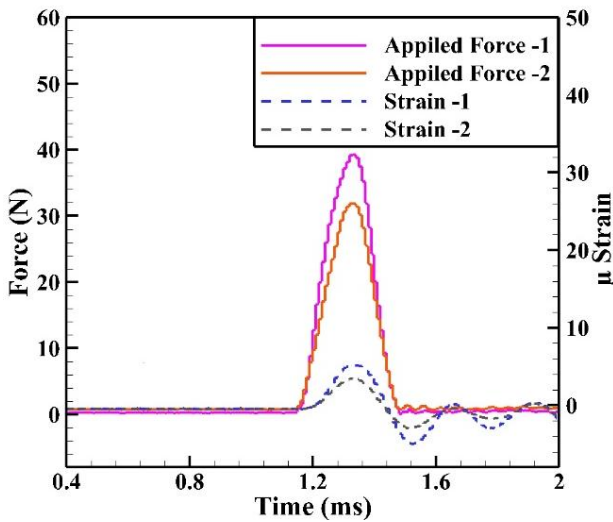


Figure 4.14 : Strain-time history to corresponding applied force for calibration experiments.

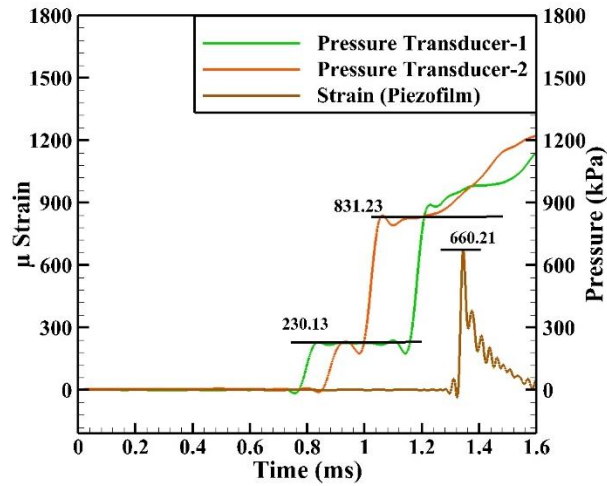


Figure 4.15: Strain-time history with pressure signals of Shock tube experiments

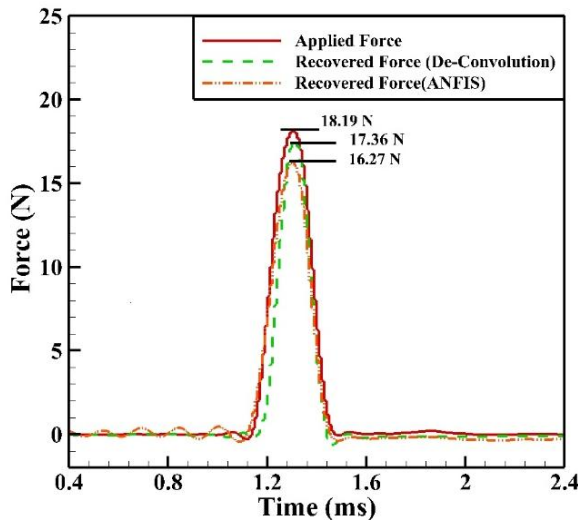


Figure 4.16: Recovered applied force for calibration experiment from different force recovery algorithms

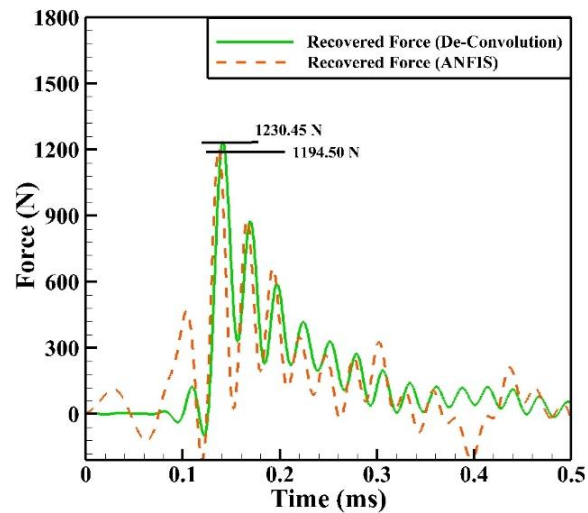


Figure 4.17: Recovered drag force for shock tube experiment from different force recovery algorithms

8. Conclusion

The shock tube facility has been designed and fabricated successfully. Then, this impulse facility was installed with proper instrumentation at the IIT Guwahati Gas Dynamic Laboratory. After successful installation, a calibration of the shock tube was performed carefully. During calibration, the shock tube parameters, such as incident shock Mach number, reflected shock Mach number, and various pressure ratios for different regions of the shock tube, were estimated successfully. These experimental data have also been compared with theoretical data of various shock tube parameters. Further, a numerical investigation has also been performed successfully to understand the flow behavior of shock travel after diaphragm bursting. And the numerically estimated incident shock Mach number has also been compared successfully with the experimental shock Mach number. In the end, this new shock tube facility has been tested by conducting the stress wave force balance-model

assembly at the shock tube end. The experimental responses has been recorded successfully in data acquisition system. After the experiment, the obtained responses are successfully fed into well-developed force recovery algorithms, and the drag force is successfully recovered from these algorithms. It is concluded from the results that the recovered drag forces from both algorithms are in agreement with the magnitude and trends of each other. So, it can also be concluded here that performed experiments in shock tube are found to be consistent. And it can be used in the future to conduct experiments under various environmental conditions.

References

- [1] Duff, R. E., & Blackwell, A. N. (1966). Explosive driven shock tubes. *Review of Scientific Instruments*, 37(5), 579-586.
- [2] Modarres, D. and Azzazy, M. (1988) 'Modern experimental techniques for high speed flow measurement', AIAA, 26th Aerospace Sciences Meeting, Nevada.
- [3] Doolan, C.J. and Morgan, R.G. (1999) 'A two-stage free piston driver', *Shock Waves*, Vol. 9, pp.239–243
- [4] Itoh, K., Komuro, T., Sato, K., Tanno, H. and Ueda, S. (2001) 'Hypersonic aerodynamic research of HOPE using high enthalpy shock tunnel', AIAA 10th International Space Planes and Hypersonic systems and Technologies Conference, pp.24–27, April, Kyoto, Japan
- [5] Stalker, R.J., Paull, A., Mee, D.J., Morgan, R.G. and Jacobs, P.A. (2005) 'Scramjets and shock tunnels – the Queensland experience', *Progress in Aerospace Sciences*, Vol. 41, pp.471–513.
- [6] Takayama K, Reddy KPJ and Kumar CS (2014), *Shock waves made simple*, Wiley India Pvt. Ltd. India.
- [7] Kunz, A., Bhaskaran, K. A., & Roth, R. (2001). *Shock Tube Study on the Reaction of Si Atoms with CH₃ with Respect to SiC Formation*.
- [8] Spadaccini, L. J., & Colket III, M. B. (1994). Ignition delay characteristics of methane fuels. *Progress in energy and combustion science*, 20(5), 431-460.
- [9] Andreotti, R., Colombo, M., Guardone, A., Martinelli, P., Riganti, G., & di Prisco, M. (2015). Performance of a shock tube facility for impact response of structures. *International Journal of Non-Linear Mechanics*, 72, 53-66.
- [10] Ray, N., Jagadeesh, G., & Suwas, S. (2015). Response of shock wave deformation in AA5086 aluminum alloy. *Materials Science and Engineering: A*, 622, 219-227.
- [11] Timoshenko, S., Timoshenko, S.P., Timoshenko, S.P. and Timoshenko, S.P. (1956) *Strength of Materials*, Vol. 210, Van Nostrand, New York.
- [12] Cobb, H. M. (2010). *The history of stainless steel*. ASM International.

- [13] Mousavi, F., Hashemi, R., & Madoliat, R. (2018). Measurement of directional anisotropy coefficients for AA7020-T6 tubes and prediction of forming limit curve. *The International Journal of Advanced Manufacturing Technology*, 96, 1015-1023.
- [14] Murty, H. S., & Gottlieb, J. J. (1984). Analytical and numerical study of the flow in a shock tube with an area change at the diaphragm section. NASA STI/Recon Technical Report N, 84, 31563.
- [15] Agarwal, S., & Sahoo, N. (2018). An experimental investigation towards calibration of a shock tube and stagnation heat flux determination. *International Journal of Aerodynamics*, 6(1), 18-40.
- [16] Sahoo, N., Mahapatra, D. R., Jagadeesh, G., Gopalakrishnan, S., & Reddy, K. P. J. (2003). An accelerometer balance system for measurement of aerodynamic force coefficients over blunt bodies in a hypersonic shock tunnel. *Measurement Science and Technology*, 14(3), 260.
- [17] Jang, J. S. (1993). ANFIS: adaptive-network-based fuzzy inference system. *IEEE transactions on systems, man, and cybernetics*, 23(3), 665-685.